



# Unveiling local atomic bonding and packing of amorphous nanophases via independent component analysis facilitated pair distribution function

Xiaoke Mu<sup>a,\*</sup>, Leyi Chen<sup>a,c</sup>, Ralf Mikut<sup>c</sup>, Horst Hahn<sup>a,e</sup>, Christian Kübel<sup>a,b,d</sup>

<sup>a</sup> Institute of Nanotechnology, Karlsruhe Institute of Technology (KIT), 76344 Eggenstein-Leopoldshafen, Germany

<sup>b</sup> Karlsruhe Nano Micro Facility, Karlsruhe Institute of Technology (KIT), 76344 Eggenstein-Leopoldshafen, Germany

<sup>c</sup> Institute for Automation and Applied Informatics (IAI), Karlsruhe Institute of Technology (KIT), 76344 Eggenstein-Leopoldshafen, Germany

<sup>d</sup> Department of Materials and Earth Sciences, Technical University of Darmstadt, 64287 Darmstadt, Germany

<sup>e</sup> Herbert Gleiter Institute of Nanoscience, Nanjing University of Science and Technology, Nanjing, China

## ARTICLE INFO

### Article history:

Received 5 February 2021

Revised 22 April 2021

Accepted 22 April 2021

Available online 26 April 2021

### Keywords:

Metallic nanoglass

Shear band

Scanning transmission electron microscopy

Local pair distribution function

Independent component analysis

## ABSTRACT

Amorphous nanophases play a significant role for the properties of a variety of nanoscale heterogeneous materials. Experimental characterization of the atomic arrangement of the amorphous structure, including nanoscale structural variations, is one of the main challenges limiting the rational design of the materials. Here, an approach to characterize local bonding and atomic packing in complex nanomaterials is introduced. Building on scanning transmission electron microscopy (STEM) and pair distribution function analysis (PDF) to record local diffraction information with nanometer spatial resolution, we show that independent component analysis for “blind source separation” of mixed information due to projection effects in STEM-PDF, enables full separation of these signals. The unprecedented information allows determining the structure of individual nanoscale phases and identifying the compounds inside. We analyzed a FeZr/ZrO<sub>2</sub> multilayer as proof of principle, and discovered differently coordinated FeO<sub>x</sub> in the interfacial region. The approach was applied to Fe<sub>25</sub>Sc<sub>75</sub> nanoglass and revealed Fe–Fe bonding concealed in the Sc-rich matrix. Finally, analysis of a shear band in a deformed Cu/CuZr nanolaminate confirmed Cu enrichment and reduced medium-range order in the shear band.

© 2021 The Authors. Published by Elsevier Ltd on behalf of Acta Materialia Inc.  
This is an open access article under the CC BY license (<http://creativecommons.org/licenses/by/4.0/>)

## 1. Introduction

The structural novelty at microscopic scale is the origin of the unique functionalities of materials. In particular, amorphous materials lacking long-range order and composite materials consisting of various amorphous phases at the nanoscale are extensively employed in material science and advanced engineering. The difficulty of experimentally measuring the atomic arrangement in the nanoscale phases is one of the major obstacles for rationalizing, understanding and tuning the material properties. For example, bulk metallic glasses (BMG), which possess excellent elasticity and strength [1], are strongly limited by their poor ductility and lack of work hardening due to localized shear band formation during plastic deformation [1,2]. However, the difficulties in charac-

terizing the structure of the material in the shear band, which is only a few nanometers wide, embedded in the matrix material, and exhibits very weak contrast in conventional characterization techniques [3,4], limits the understanding of shear band formation and hence the deformation mechanisms of BMGs. Nanostructured metallic glass-composites (i.e. nanoglasses) [5,6], consisting of multiple amorphous phases at the nanoscale, have been introduced as an approach to further tailor the properties of metallic glasses (MGs), e.g. to suppress shear band formation, and resulted in MGs with exceptional physical, e.g. magnetic, properties [7,8]. The unique behavior of nanoglasses are speculated to be due to the nanoscale (structural/chemical) phase separation and related changes in atomic short-range order [9,10]. However, a clear correlation of the properties with the nanoglass structure has been limited so far by the challenges in appropriate characterization of the individual glassy phases. Therefore, it is essential to develop capa-

\* Corresponding author.

E-mail address: [xiaoke.mu@kit.edu](mailto:xiaoke.mu@kit.edu) (X. Mu).

bilities to accurately characterize heterogeneous amorphous materials.

Pair distribution function (PDF) analysis based on X-ray diffraction is typically used to characterize the average bulk structure of amorphous materials [11]. PDF analysis measures the interatomic distances and atomic coordination, giving the most directly interpretable information on the short- and medium-range order in amorphous materials. (Scanning) transmission electron microscopy (S/TEM) methods can provide more local information. Electron PDF (ePDF) analysis based on selected area electron diffraction (SAED) can be performed analogously to X-ray diffraction experiments providing a spatial resolution down to the sub hundred nanometer level [12,13]. Fluctuation electron microscopy (FEM) measures structural variations in a material by measuring the variance of intensities either based on nanobeam electron diffraction patterns or based on hollow-cone dark-field images obtained with varying tilting angles [14]. FEM is highly sensitive to the medium-range order in amorphous materials and has been applied e.g. to compare the averaged structural difference between shear bands and undeformed matrix in MGs [15]. However, FEM typically requires comparison with molecular modeling for a detailed structural interpretation [16,17], and the variance measured by FEM represents averaged properties of the sampled material. In order to perform a local analysis, intensity variations along azimuthal angles of individual diffraction patterns acquired by 4-dimensional STEM (4D-STEM), can give insights into the rotational symmetry of local atomic clusters in MGs [18,19]. However, the analysis requires minimal overlap of clusters, even of the same type in a single phase, otherwise the result suffers severely from nonlinear degradation [18]. A recent attempt to overcome the challenges in characterizing nanoscale heterogeneous amorphous materials is the development of STEM-PDF [20,21]. It uses PDF to analyze 4D-STEM data to map the local PDF of materials thereby realizing structural analysis and phase mapping with a spatial resolution down to one nanometer. PDF is relatively robust against sample thickness variations for measuring the interatomic distances and their relative contributions to the structure [22,23]. However, for nanocomposites where the size of at least one of the phases is less than the thickness of the sample, e.g. in nanoglasses or embedded shear bands, the “projection problem” renders the local PDF a mixture of the individual phases the electron beam is propagating through. In addition, the finite collection angle of the electron diffraction pattern intrinsically limits the  $r$ -resolution for PDF analysis, resulting in a separation problem for peaks representing similar atomic distances in the PDF. Important structural information, e.g. specific bond length and coordination of the embedded amorphous phases, is diluted or even hidden by the overlapping signals, giving rise to huge difficulties in studying hetero-structured amorphous materials such as shear bands and metallic nanoglasses.

In this work, we demonstrate that by combining STEM-PDF with independent component analysis (ICA) the PDFs of embedded nanophases, which are entangled with each other and cannot be probed individually, can be separated from the mixed signals. The resulting independent PDFs contain the true structural information of the individual phases in terms of atomic bonding, atomic coordination and packing as concrete representation of the local short- and medium-range order. This information enables identification of the chemical compounds inside the nanophases and enables characterization of the extent of their ordering. As proof of principle, we tested the approach by characterizing the interface of an amorphous  $\text{ZrO}_2/\text{FeZr}$  multilayer, which demonstrates the high sensitivity of the method to detect hidden local structures at the interface. We then applied it to investigate the nanophases in an  $\text{Fe}_{25}\text{Sc}_{75}$  nanoglass and studied the atomic packing in a shear bands in a deformed amorphous-CuZr/crystalline-Cu (a-CuZr/c-Cu) nanolaminate.

## 2. Experimental

### 2.1. Sample preparations

The amorphous  $\text{ZrO}_2/\text{ZrFe}$  multilayer has been prepared by magnetron sputtering with separate  $\text{ZrO}_2$  and ZrFe targets. A cross-section of the  $\text{ZrO}_2/\text{ZrFe}$  multilayer sample for TEM analysis was prepared by focused ion beam (FIB) (ZEISS Auriga 60) and further thinned by low-voltage argon ion-milling (Fischione Nanomill 1040). The final sample thickness is around 0.4 inelastic mean free path (MFP) determined by low-loss EELS analysis, corresponding to 50 nm sample thickness based on the average MFP calculated using Mitchell's DM plugin “mean free path estimator” [24]. The Zr: Fe ratio is 2: 8 as measured by EDX.

$\text{Fe}_{25}\text{Sc}_{75}$  nanoparticles of approximately 7 nm diameter were produced by inert gas condensation (IGC); details can be found in [8]. Disk-like  $\text{Fe}_{25}\text{Sc}_{75}$  nanoglass pellets were produced by in situ consolidation of the glassy nanoparticles at 2 GPa and further by ex situ consolidation at 6 GPa. TEM lamella of the pressed nanoglass were prepared by FIB with the thickness of 25 nm measured by low-loss EELS.  $\text{Fe}_{25}\text{Sc}_{75}$  and  $\text{Fe}_{90}\text{Sc}_{10}$  BMG were prepared by melt-spinning. TEM lamella of the ribbons were prepared by FIB with a thickness about 50 nm (measured by low-loss EELS), which is about twice the thickness of the nanoglass lamella. This significantly weakens contributions due to surface oxidation in the BMG lamellae. The Fe: Sc of the samples was confirmed by EDX and EELS.

The a-CuZr/c-Cu nanolaminate is produced by magnetron sputtering pure Cu and Zr targets (99.99 at.%) alternately on Si (100) wafer with thickness of 100 nm for a-CuZr and 10 nm for c-Cu. The total thickness was around 1200  $\mu\text{m}$ . The FIB lamella with a thickness about 50 nm (measured by low-loss EELS) was lifted out after indentation with a 10 g Vickers indenter for 10 s. More details can be found in reference [25]. The Cu to Zr ratio of 1:1 in the amorphous layer was confirmed by EDX.

### 2.2. Scanning electron diffraction (4D-STEM)

The scanning electron diffraction (4D-STEM) experiments for STEM-PDF were performed using a Tecnai F20 ST (Philips) operated at 200 kV in microprobe STEM mode with spot size 8, gun lens 6, extraction voltage of 4.5 kV and a 30  $\mu\text{m}$  C2 aperture resulting in a semi convergence angle of 1.3 mrad. A camera length of 100 mm was used, and a 0.6 degree beam precession produced by NanoMegas Top-Spin system [26] was applied for pushing the largest recorded diffraction angle to  $2\theta > 50$  mrad ( $s_{\text{max}} = 2\theta/\lambda > 2.0 \text{ \AA}^{-1}$ ), where  $\theta$  is the scattering semi-angle and  $\lambda$  is the wavelength of the incident electrons. These settings result a probe size of approximately 1.5 nm. To optimize the spatial resolution for the FeSc nanoglass sample, the precession was switched off and the effective  $s_{\text{max}} > 1.7 \text{ \AA}^{-1}$ . The beam scanning and 4D-STEM data acquisition was driven by the NanoMegas Top-Spin system equipped with a Stingray CCD camera with  $580 \times 580$  pixels, which captures the diffraction patterns on the binocular viewing screen with 0.05 s exposure time for each pattern. Virtual annular dark field (ADF) images were created from the 4D-STEM data by choosing a virtual detector defining the collection angle  $\beta$  of 28.0–48.5 mrad for each of the diffraction patterns.

### 2.3. Conventional S/TEM

STEM EELS and EDX measurements were performed using an aberration (image) corrected Titan 80–300 (FEI Company), equipped with a Gatan Tridium 863 image filter (GIF) and operated at 300 kV, 30  $\mu\text{m}$  condenser C2 aperture and camera length of

38 mm resulting in a convergence semi angle of 14 mrad and a collection angle of 15 mrad. Selected area electron diffraction (SAED) to determine the average PDFs of the FeSc BMGs was performed in TEM mode with the illumination convergence angle of <0.1 mrad and an area of 1.5  $\mu\text{m}$  diameter selected by using a 50  $\mu\text{m}$  condenser (C2) aperture. The recorded maximum scattering angle was 60 mrad, corresponding to 3  $\text{\AA}^{-1}$  in reciprocal space.

## 2.4. STEM-PDF processing

Figure S1 describes the PDF analysis of the local diffraction pattern from the 4D-STEM data. Each 2D diffraction pattern is azimuthally integrated to yield 1D diffraction profiles  $I(s)$ . Following the procedure in [12,20], the diffraction profiles are normalized to  $\varphi(s) = \frac{I(s) - N\langle f(s)^2 \rangle}{N\langle f(s)^2 \rangle} s$ ,  $\langle f(s)^2 \rangle$  is the averaged atomic scattering factor of all elements contributing to the diffraction pattern, and is calculated using the average composition obtained from the EDX or EELS analysis.  $N$  is the number of atoms irradiated by the electron beam and determined by matching  $\langle f(s)^2 \rangle$  at  $s_{\text{max}}$ .  $\varphi(s)$  is often referred to as structure factor, describing the structural information in reciprocal space. The PDFs are obtained by Fourier sine transformation of  $\varphi(s)$ , through  $\text{PDF}(r) = \int_0^{s_{\text{max}}} \varphi(s) \sin(2\pi sr) ds$ . As illustrated in Fig. 1a, the array of PDFs are then arranged to create a PDF data cube according to the scan sequence of the 4D-STEM patterns.

In practice, due to multiple elastic scattering and inelastic events, the calculated  $\langle f(s)^2 \rangle$  often cannot match the experimental diffraction profiles at both small and large angles simultaneously. Figure S2 shows an example of processing a nanobeam electron diffraction pattern arbitrarily picked from the  $\text{ZrO}_2$  layer in the amorphous  $\text{ZrO}_2/\text{FeZr}$  multilayer specimen. The amorphous structure does not have defined atomic columns as in crystals, so that elastic scattering in an amorphous sample does not exhibit any “channeling” phenomenon, instead, it can be described by multiple self-convolutions of the 2D kinetic diffraction pattern [23]. Therefore, multiple scattering does not introduce additional structural information into the diffraction pattern except that it contributes to a smooth background to the diffraction intensity and causes strong oscillation at low- $r$  and reduction of the absolute intensity in the PDF [22,27]. Nevertheless, the method analyzes the relative variation of diffraction patterns in the 4D-STEM data. A comparable multiple scattering situation at different sample location is expected for FIB specimen with moderate thickness variations. An examination of a wedge-shaped  $\text{Pd}_{85}\text{Si}_{15}$  glass has been performed to experimentally evaluate the robustness of the PDF against strong sample thickness variation. It was found that the shift of the 1st peak (Pd–Pd bond at 2.84  $\text{\AA}$ ) is within 0.01  $\text{\AA}$  (0.35%) when the sample thickness doubles from 30 nm to 60 nm. This thickness variation is magnitudes larger than any variation in the examples shown in this work. The artifact of low- $r$  oscillation can be effectively suppressed by subtracting a polynomial function (4th to 6th order) from  $\varphi(s)$  (Figure S2B, red curve) [22], which also eliminates issues with the local scattering factor deviating from the average due to compositional fluctuations as demonstrated in [20]. The polynomial corrected  $\varphi(s)$  (Figure S2C, blue curve) is then smoothed by local regression with a 2<sup>nd</sup> degree polynomial model, followed by a Gaussian damping at large angles (Figure S2C, red curve) to reduce noise before the Fourier transformation. Figure S3 shows example PDFs with  $r$  starting from 0 obtained from the nanobeam diffraction pattern arbitrarily taken from the nanoglass and CuZr nanolaminate sample.

As a convergent beam has to be employed to form a nano-sized probe for local PDF measurements, the angular resolution in the nano-diffraction pattern is reduced due to convolution with the

convergence angle, which dampens the PDF at high- $r$ . Applying a deconvolution to the diffraction patterns [28–30] with careful evaluation of the deconvolution artifacts could potentially minimize this information damping. For a better comparison between the SEAD PDF and STEM-PDF, the SEAD patterns taken from the FeSc BMGs were convolved with a 2.6 mrad flat disk before calculating the PDF to mimic the convergence angle of the electron beam in the STEM-PDF experimental setup, and the maximum diffraction angle was cut at 2  $\text{\AA}^{-1}$  in the PDF calculation to resemble the STEM-PDF acquisition. The same truncation angle was applied in the PDF simulation (Fig. 1h) to simulate the experimental limitations.

To evaluate the error in the bond length measurement using STEM-PDF, the statistic fluctuations of the peak position in the PDF data cube are estimated looking at the standard deviation of the 1st peak position using the data taken from the pure  $\text{ZrO}_2$  and FeZr layer in the  $\text{ZrO}_2/\text{FeZr}$  multilayer dataset. The average 1st peak positions for the  $\text{ZrO}_2$  and FeZr layers are 2.08  $\text{\AA}$  and 2.48  $\text{\AA}$ . Their standard deviations are 0.008  $\text{\AA}$  (0.24%) and 0.006  $\text{\AA}$  (0.38 %), providing an idea of the small structural variations that could be detected within a single STEM-PDF data set. The main error for the bond length determination comes from the systematical error in the camera length calibration, which is typically in the range of 1–2 %.

## 3. Results and discussion

### 3.1. Proof of principle

Fig. 1a schematically describes the STEM-PDF data acquisition and analysis. The PDFs represent atomic pair correlations as a function of pair distance  $r$  and thus enable interpretation of the information encoded in the local diffraction data in terms of bond length, atomic coordination and packing. The PDFs are arranged according to the scanning sequence to form a PDF data cube as a type of hyperspectral image. A  $\text{ZrO}_2/\text{FeZr}$  multilayer (Fig. 1) is used for a proof of principle to establish the combination of STEM-PDF and ICA analysis because of the simple geometry and the established previous knowledge about the material [20]. The bright layers in the high angle annular dark field (HAADF) STEM image correspond to the FeZr metallic glass and the darker ones correspond to the amorphous  $\text{ZrO}_2$ . The STEM-PDF data cube is obtained from the area highlighted by the dashed box in Fig. 1b (left). Fig. 1c shows PDFs directly taken from the data cube in the region belonging to the FeZr and the  $\text{ZrO}_2$  layer and the interfacial region (colored dashed boxes in Fig. 1b (right)). We can see that, although the PDF taken from the interfacial region (red dashed line, Fig. 1c) shows features very close to the PDF of the  $\text{ZrO}_2$  layer (green solid line, Fig. 1c), a slight left-shift of the 1st peak compared to the PDF of the  $\text{ZrO}_2$  layer (highlighted in the inset of Fig. 1c) implies that the average bond length in the interfacial region is shorter than the Zr–O distance in the  $\text{ZrO}_2$  layer. Obviously, a secondary phase in addition to  $\text{ZrO}_2$  is present at the interfacial layer. By using EELS and EDX analysis, we can deduce the interfacial region consists of Fe, Zr and O. However, the key questions, which compound the secondary phase corresponds to, what kind of atomic bonding/arrangement is present and whether all three elements contribute to the interface phase, cannot be answered with the current information. This information is hidden in the local PDF of the interfacial region where the mixed signal is dominated by the  $\text{ZrO}_2$  phase. We are going to demonstrate below that applying ICA to the STEM-PDF data can disentangle the information of the unknown interfacial phase from the mixed signal and therefore unveil the structure/chemistry of the amorphous nanophase.

To model the signal mixing, the STEM-PDF data cube can be represented by a 2D matrix  $\mathbf{X}$ , where the rows are experimentally

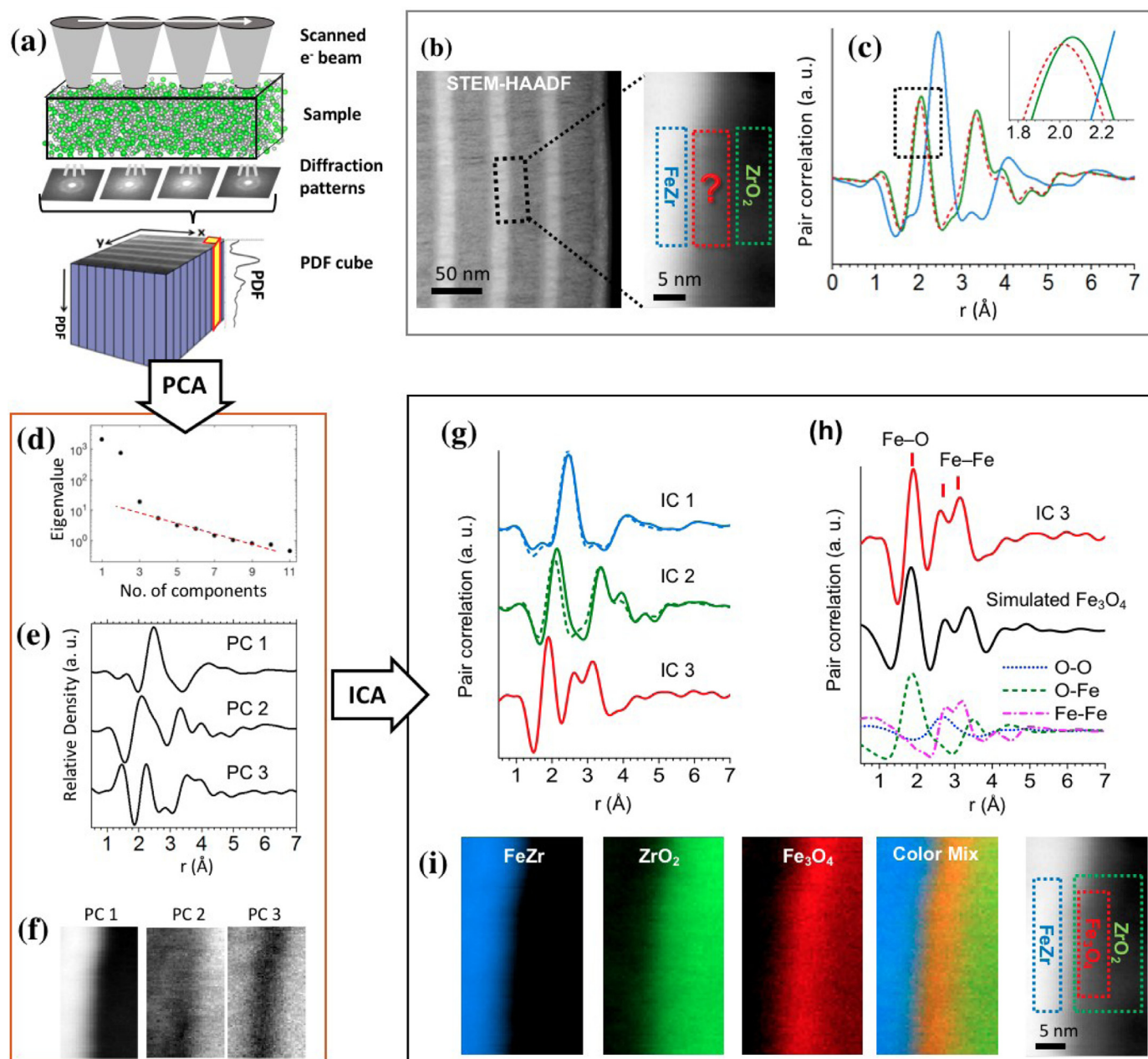


**Fig. 1.** Test ICA facilitated STEM-PDF for characterizing amorphous nanoscale multilayer. (a) Schematic depiction of STEM-PDF (reproduced with permission [21], 2018, WILEY-VCH). (b) Left: conventional STEM-HAADF image of the amorphous ZrO<sub>2</sub>/FeZr multilayer. Right: virtual annular dark field (ADF) image obtained from the 4D-STEM data. (c) PDFs of FeZr layer (blue line), ZrO<sub>2</sub> layer (green line) and the interfacial region (red dashed line) taken from the area indicated by the corresponding colored boxes in (b, right). PCA results in the (d) screen plot, (e) The first 3 PCs, and (f) their spatial distributions. (g) ICs (solid lines) resulted from ICA analysis of the PCA results, where IC1 and IC2 are compared to the raw PDFs of the FeZr layer (blue dashed lines) and ZrO<sub>2</sub> layer (green dashed lines) taken from Figure 1c. (h) Comparison of IC3 (red solid line) and a simulated PDF based on crystalline Fe<sub>3</sub>O<sub>4</sub> [40] (Marokite, solid black line) and its partial PDFs. (i) Distribution map of the ICs (i.e. IC coefficients) and their correlation with the virtual ADF image. (For interpretation of the references to color in this figure legend, the reader is referred to the web version of this article.)

measured PDFs at different sample locations and columns correspond to the atomic pair distance  $r$  (in units of Å in this paper). In a good approximation, the experimental local PDFs obtained by STEM-PDF can be considered as a linear combination of PDFs from the individual phases. The mixed signal therefore can be modeled as a matrix multiplication  $\mathbf{X} = \mathbf{AS}$ , where the rows of matrix  $\mathbf{S}$  represent the PDFs of the pure phases.  $\mathbf{A}$  is a matrix and its elements are weighting factors to describe how the pure phase PDFs are mixed in  $\mathbf{X}$ . To solve for the independent phases and their distribution only knowing  $\mathbf{X}$ , we perform a “blind source separation” to determine the source  $\mathbf{S}$  and the weighting factors  $\mathbf{A}$  by using ICA [31].

The first step is to identify the number of uncorrelated components in  $\mathbf{X}$ , namely to find the number of rows in  $\mathbf{S}$ . This can be achieved by principal component analysis (PCA) of the data  $\mathbf{X}$  as preprocessing for ICA. PCA has been used to denoise 3D spectrum image data in electron energy loss spectroscopy (EELS) [32,33] and energy dispersive X-ray spectroscopy (EDX) [34], as well as tested to group 4D-STEM patterns for PDF analysis [35]. This PCA preprocessing is also called data whitening. It finds matrices  $\mathbf{W}$  and  $\mathbf{U}$  making  $\mathbf{X} = \mathbf{WU}$ , where the rows of  $\mathbf{U}$  represents the principal components (PCs) (i.e. principal PDFs, also called “loadings”) and  $\mathbf{W}$  is whitening matrix (also called “scores” of the loadings), the columns of which are the eigenvectors of the covariance matrix

( $\mathbf{X}\mathbf{X}^T$ ,  $T$  denotes transpose) and represent the spatial distributions of the PCs (i.e. the map of the PCs). The raw PDFs ( $\mathbf{X}$ ) are then represented as a linear combination of the principal PDFs. The corresponding eigenvalues of the covariance matrix ( $\mathbf{X}\mathbf{X}^T$ ) describe the statistical variance of each PC and represent their occupation in the data. In this work the PCA was performed by singular value decomposition using the matlab function “svd()”.

The first 3 PCs and corresponding distribution maps using the amorphous ZrO<sub>2</sub>/FeZr as example are shown in Fig. 1e and f. The so-called “scree plot” of the eigenvalues is shown in Fig. 1d on a logarithmic scale (linear scale in Figure S4) in descending order. Usually noise decreases exponentially with increasing component order [32], so that the low-order components above the red dashed line in Fig. 1d can be considered as meaningful principal components [33,36,37]. In the current sample with very simple geometry, the scree test delivers a clear conclusion that  $\mathbf{X}$  contains 3 significant PCs (Fig. 1e) corresponding to three phases with distinct structures in the measured sample area. It will be seen in the following application examples, complex phase distribution and strong mixing will corrupt the scree plot, judgment of the number of the principal components only using eigenvalues in the scree test can be difficult. However, we are going to show in Determining Number of Components (Section 7) that random noise in the dewhiting matrix (PC maps) and the high-order component curves provide effective information to separate the physically meaningful components from artifacts. We use local information entropy to quantify the information/noise in the PC maps (higher level of random noise means less meaningfulness of the corresponding component and leads to higher entropy) and use this quantity to weight the eigenvalues for scree test. The adapted scree test enables confident determination of the number of components for complex samples with strong phase mixing.

All PCs are orthogonal to each other (i.e.  $\mathbf{E}\{\mathbf{u}_i \cdot \mathbf{u}_j\} = 0$  when  $i \neq j$ , where  $\mathbf{E}\{\}$  means mathematic expectation and  $\mathbf{u}_i$  is the  $i$ th row of  $\mathbf{U}$ ) and oriented along the direction maximizing their variance (i.e.  $\max(\mathbf{E}\{\mathbf{u}_i^2\})$ ). However, PCs may nonlinearly correlate with each other at higher-order statistics, e.g.  $\mathbf{E}\{\mathbf{u}_i^n \cdot \mathbf{u}_j^n\} \neq 0$  when  $i \neq j$  and  $n > 1$ , meaning PCA does not guarantee statistical independence of PCs. PCs may still represent mixtures of pure sources and cannot necessarily be meaningfully interpreted as material representation. As shown in Fig. 1e, PC2 deviates from the PDF of the pure ZrO<sub>2</sub> phase. Furthermore, the spatial distribution of the PCs (Fig. 1f) cannot be directly interpreted. More recently, non-negative matrix factorization (NMF) [38], another variant of the multivariate statistical analysis family PCA belongs to, has been used to solve overlap problems of 2D crystalline diffraction patterns from 4D-STEM data to realize 3D orientation mapping of a polycrystalline material [39]. NMF looks for the solution of  $\mathbf{X} = \mathbf{A} \cdot \mathbf{S}$  by using a simple positive constrain of  $\mathbf{A}$  and  $\mathbf{S}$  without consideration of mutual correlation of the data. NMF works well for sparse data e.g. EDX and spot diffraction patterns, but does not work for PDF of amorphous structures, which is a continuous function, oscillating around “0” representing pair correlations relative to the average. In contrast, ICA, which was developed for blind source separation considering higher order statistics [31] and has been applied e.g. for EELS spectral image analysis [36], fits well to PDF-type data. ICA uses the concept that the probability density function of a signal is closer to Gaussian distributed the more sources are mixed in the signal. Deviations from the Gaussian distribution (non-gaussianity) are therefore a measurement of the independence of the signals and can be quantified by nonlinear statistics (e.g. the higher order cumulants of the probability density function of the signals than covariance). ICA optimizes a rotation matrix  $\mathbf{R}$ , which rotates the PCs making  $\mathbf{S} = \mathbf{R}\mathbf{U}$ , until the resulting components (rows of  $\mathbf{S}$ ) exhibit the highest deviation from the

Gaussian distribution, thus get statistically independent from each other. The rows of  $\mathbf{S}$  are the independent components (ICs) representing the PDFs of the individual, demixed phases of the mixture. In this work, ICA was performed by the FastICA matlab code (<https://www.cs.helsinki.fi/u/ahyvarin/whatisica.shtml>) [31].

Fig. 1g and i show the resulting ICs and their spatial distribution. IC1 and IC2 can be interpreted straightforwardly in good agreement with the PDFs of FeZr and ZrO<sub>2</sub>. IC3 corresponds to the PDF of the minor interfacial phase containing much more information than the PDF directly taken from the interfacial region (red dashed line in Fig. 1c). IC3 matches very well with the PDF simulated based on the short-range order in Marokite-type crystalline Fe<sub>3</sub>O<sub>4</sub> (space group Pbcm [40]). The 1st peak of IC3 at 1.90 Å corresponds to the Fe–O bond length. The 2nd and 3rd peak at 2.61 and 3.15 Å fit Fe–Fe correlations (as shown by the Fe–Fe partial PDF, pink dash-dot line in Fig. 1h), which suggests two different Fe environments fitting well to FeO<sub>x<5</sub> polyhedral and FeO<sub>6</sub> octahedral coordination. As no Zr–X (X = Fe or O) related features are observed, the PDF reveals that the Zr atoms do not participate in this compound. All this shows that the compound constituting the phase in the interfacial region is Fe<sub>3</sub>O<sub>4</sub>, which does not only exist directly at the interface, but also permeates into the bulk ZrO<sub>2</sub> layer (Fig. 1i, red). The weak but detectable difference between IC2 and the PDF of the bulk ZrO<sub>2</sub> layer (green dashed line in Fig. 1g) is attributed to this mixing. It is worthwhile noting that ICA is a reference-less procedure in contrast to the MLLS fitting.

One might notice, that the FeZr phase is well separated from the other phases and the iron oxide phase is concentrated at the interface giving rise to a simple situation. This renders PC1 mostly identical to IC1 and PC3 similar to the inverted IC3. We will see in the investigation of the following examples, that PCs can contain strongly mixed information and cannot necessarily be associated with individual phase at all.

### 3.2. Application to metallic nanoglass

Nanoglasses can be synthesized by consolidation of amorphous nanoparticles, e.g. produced by inert gas condensation (IGC). The surface of the glassy nanoparticles is expected to be modified during deposition/compacting to form a “shell” phase exhibiting different short-range order and/or chemical composition compared to the “core” [10]. After compacting the nanoparticles under high pressure in the range of several GPa, the metallic nanoglass is supposed to consist of two different amorphous phases with characteristic dimensions of a few nanometers [5,6]. A Fe<sub>25</sub>Sc<sub>75</sub> nanoglass has been shown to possess superior ductility [6,41] and enhanced ferro-magnetic properties [8] at low temperatures compared to its bulk metallic glass counterpart. These have been speculated to be due to the existence of two phases, possibly with Fe concentrating in one of them. In this section, we apply the ICA facilitated STEM-PDF to analyze the structure of the Fe<sub>25</sub>Sc<sub>75</sub> nanoglass.

A 4D-STEM data set is taken from a FIB lamella of the nanoglass (Figure S5). Visual analysis of the STEM-PDF data indicates two types of PDFs (Fig. 2b). One is corresponding to a Fe-rich (red) and the other one is a Sc-rich phase (green). The 2nd and 3rd peak at 2.84 Å and 3.30 Å are attributed to the Fe–Sc and Sc–Sc metallic bonds, and the 1st peak at 2.18 Å potentially corresponds to metal (Fe or Sc) to oxygen bonds, which is more pronounced in the Sc-rich phase. A two-phase map (Fig. 2c) was derived using the manually selected two PDFs as references for MLLS fitting to the STEM-PDF data cube. The oxidation (15 at.% in average (Figure S6)) is attributed to diffusion of oxygen from air into the FIB prepared TEM lamella which has a thickness of 0.2 inelastic MFP, around 25 nm, measured by the EELS log-ratio method.

The average size of the nanoparticles used to produce the nanoglass is about 7 nm. This is ~3.5 times smaller than the thickness

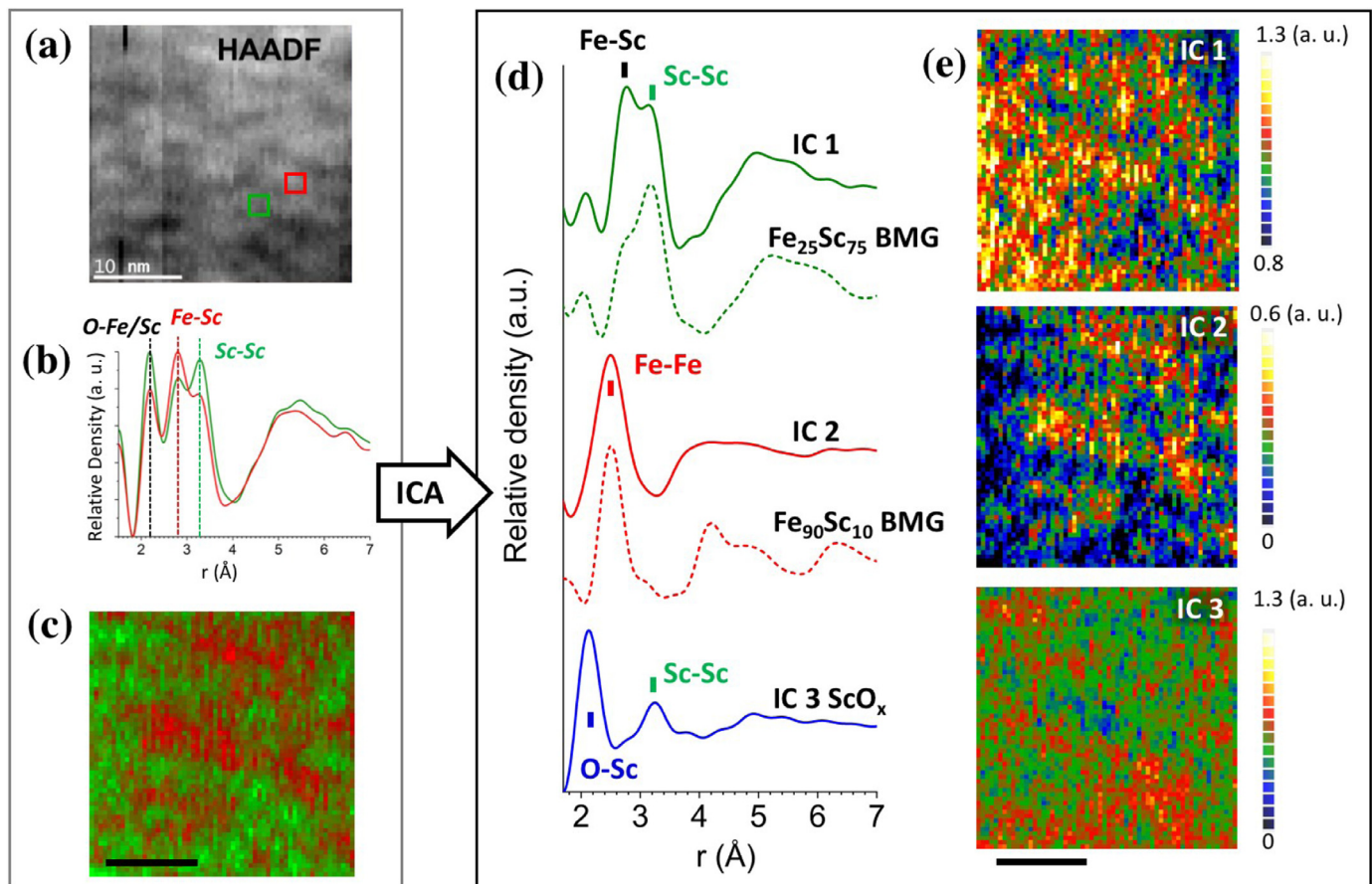


**Fig. 2.** ICA facilitated STEM-PDF characterizing FeSc nanoglass. (a) Virtual ADF image obtained from the 4D-STEM data set. (b) Reference PDFs manually selected from the STEM-PDF data cube corresponding to the red and green boxes in (a), indicating a Fe-rich (red) and a Sc-rich (green) phase. (c) Spatial distribution of the two phases by MLLS fitting using the two reference PDFs in (b). (a–c) are reproduced with permission [6] 2018, WILEY-VCH. (d) ICs (solid lines) and PDFs of  $\text{Fe}_{25}\text{Sc}_{75}$  BMG (green dashed line) and  $\text{Fe}_{90}\text{Sc}_{10}$  BMG (red dashed line). (e) Spatial distribution of the individual phases (i.e. the IC coefficients in arbitrary units). The length of the scale bars in (c) and (e) are 10 nm. (For interpretation of the references to color in this figure legend, the reader is referred to the web version of this article.)

of the TEM lamella used in this experiment. This means that the electrons penetrate through several primary compacted nanoparticles in the lamella before leaving the sample. Therefore, the information carried by the electrons is typically a mixture of both phases. While the two-phase map and the elemental maps measured by STEM-EELS SI reveal elemental segregation (Figure S6), critical questions cannot be answered: (i) Is there any biased pre-judgment in the manual selection of the reference PDFs? (ii) What is the atomic arrangement in each phase? To answer these questions, ICA is applied to the STEM-PDF data cube. Interestingly, PCA as preprocess reveals three significant phases instead of the two phases manually identified (details in Determining Number of Components and Fig. 6b). More complex than the  $\text{ZrO}_2/\text{FeZr}$  multilayer, all phases are mixed in the nanoglass sample. The resulting PCs (PC1 to PC3 in Fig. 5d) cannot be interpreted directly, especially for the PC1 which actually represents the average PDF of the whole data cube. However, after ICA transforming the PCs to ICs (Fig. 2d), the underlying physical meaning of each phase becomes obvious:

I The 1st peak of IC1 (green solid line) at 2.77 Å and its shoulder at 3.18 Å are in line with the metallic bonding of Fe–Sc and Sc–Sc. The good match of IC1 and the PDF of a  $\text{Fe}_{25}\text{Sc}_{75}$  BMG (green dash line), particularly in the medium-range order ( $r > 3.5$  Å), indicates that the IC1 phase corresponds to a Sc-rich metallic phase with a structure similar to the  $\text{Fe}_{25}\text{Sc}_{75}$  BMG. The slightly lower Sc–Sc peak in IC1 compared to the  $\text{Fe}_{25}\text{Sc}_{75}$  BMG suggests that the Sc concentration in the IC1 phase is lower than the nominal value of 75 at.% of the BMG.

The distribution of IC1 phase is shown by the map in Fig. 2e, top.

- II The 1st pronounced peak of IC2 (red solid line) at 2.50 Å agrees well with the Fe–Fe bond length, while no peaks corresponding to the Fe–Sc and Sc–Sc distances are observed, suggesting that this phase is mainly constituted by Fe. Furthermore, IC2 matches well with the PDF of an  $\text{Fe}_{90}\text{Sc}_{10}$  BMG (red dash line) implying a similar structure and suggesting the Fe: Sc ratio of this IC2 phase is probably close to 90: 10. IC2 is more strongly damped at large  $r$  compared to the PDF of the  $\text{Fe}_{90}\text{Sc}_{10}$  BMG, indicating a significantly reduced (medium-range) order in the IC2 phase compared to the melt spun ribbon of  $\text{Fe}_{90}\text{Sc}_{10}$  BMG. The distribution map (Fig. 2e, middle) shows this IC2 phase distributed as clusters with sizes of 2 to 5 nm. Important features of this IC2 phase are completely hidden in the individual PDFs of the STEM-PDF data due to the “projection issue”. Nevertheless, they are clearly revealed after ICA analysis.
- III IC3 represents a scandium oxide ( $\text{ScO}_x$ ) phase, as the peak at 2.13 Å is in line with typical Sc–O bond distances and the peak at 3.25 Å corresponds to Sc–Sc bonds, whereas no Fe–Fe distance is observed in this phase. The oxide phase is quite significant in the sample, presumably due to oxidation of the very thin TEM sample. Although both Sc and Fe are very oxidation sensitive, IC3 indicates the expected preferential oxidation of Sc over Fe and that the oxidized phase is present alone separately from the Fe- and Sc-rich metallic phases. IC3 has a fairly homogeneous spatial distribution with slight anti-correlation to both

IC1 and IC2 (Fig. 2e, bottom). The EELS fine structure of the Sc-L edge taken from the sample (Figure S7) confirms that the majority of Sc is in metallic state. All these suggest that the oxide which was formed during the specimen preparation and transfer is limited to the surface and should not significantly alter the structure of the sample. The formation of the  $\text{ScO}_x$  phase is not the driven force of the Sc and Fe segregation but a consequence.

The two manually selected PDF references in Fig. 2b are mixtures of the three ICs. These mixtures would lead to the conclusion of “only two phases that are in the sample”. However, ICA analysis has shown that this does not fully reflect the truth for this sample. Most remarkably, the analysis revealed Fe–Fe bonding, proving the existence of a  $\text{Fe}_{90}\text{Sc}_{10}$ -like phase, which could hardly be detected by conventional analysis. The composition of the “ $\text{Fe}_{90}\text{Sc}_{10}$ ” phase coincides well with the eutectic point of the FeSc alloy ( $\gamma$ -Fe and  $\beta$ - $\text{Fe}_2\text{Sc}$ ) [42], suggesting a thermodynamically controlled phase separation in the nanoglass. The Sc-rich metallic phase is more homogeneously distributed than the Fe-clusters, acting as the matrix in the nanocomposite. The observed Fe clustering and existence of direct Fe–Fe bond improves our insights in the structure of the nanoglass. The results potentially explain the observed magnetic contribution to the low-temperature heat capacity in the Sc-rich nanoglass and its higher magnetization compared to the BMG counterpart [8].

### 3.3. Application to shear bands

Nanolaminate composites designed to consist of alternating layers of crystalline and amorphous metallic phases have been proven to be a promising structure for balancing both high strength and ductility [43,44]. The deformation of metallic amorphous-crystalline nanolaminates involves shear banding of the amorphous phase. Efforts were focused on understanding the chemical mixing in the shear bands [25]. However, a detailed structural characterization of the shear bands is still missing for a comprehensive understanding of the deformation mechanism. Here, we applied the ICA facilitated STEM-PDF to analyze the structure of a shear band in an a-CuZr/c-Cu nanolaminate, which was deformed by Vickers indentation as illustrated in Fig. 3a. As revealed in a previous atom probe tomography (APT) investigation, during shear banding Cu atoms are dragged from the c-Cu layer into the a-CuZr layer [25]. Shear bands with a higher Cu concentration than the surrounding matrix form in the a-CuZr layer and are located along the offsets where the c-Cu layers are broken. An example is shown in Fig. 3b, where a barely visible brighter line in the HAADF (<0.7 % in contrast) corresponds to the shear band. Representative raw PDFs taken from the shear band and the amorphous matrix region (dotted and solid black boxes in Fig. 3b) are shown in Fig. 3c. The information about the atomic correlations is strongly overlapped in the PDFs. Cu–Cu, Cu–Zr and Zr–Zr bond lengths only give rise to a single peak (the 1st peak) at 2.67 Å for the matrix and 2.58 Å for the shear band. The left shift of the peak in the PDF of the shear band suggests slightly closer atomic distances in the shear band compared to the matrix in agreement with a copper enrichment. ICA analysis is performed using the PDFs in the area of the orange dashed box in Fig. 3b. PCA, as preprocessing for the ICA analysis, results in three components (details are described in Determining Number of Components and Fig. 6c). While the PC curves (Figure S8) do not have a direct physical meaning, the ICA solution (Fig. 3d) enables a clear interpretation of the STEM-PDF data.

The shear band is clearly visible in the ICA maps (Fig. 3e–g), significantly more obvious than in the HAADF image. In contrast to the single brighter line in the HAADF image (Fig. 3b), a more complex lateral structure of the shear band is noticeable, which

**Table 1**

The 1st peak position of ICs compared to the bond lengths obtained from X-ray diffraction and MD simulation.

$r$ (Å)	ICA STEM-PDF	X-ray [47]	MD [49]
Cu–Cu	2.46	2.48	2.58
Cu–Zr	2.76	2.72	2.78
Zr–Zr	3.14	3.12	3.20

is visible in the intensity profile shown in the inset of Fig. 3e–g. It seems that the shear band contains side bands in addition to the dominant band, which is probably associated with a complex shearing mechanism [45,46].

Comparing the ICs to X-ray diffraction [47,48] and molecular dynamic (MD) simulation [49,50] based PDFs (Table 1 and Fig. 3d), it can be seen that the atomic correlations are disentangled in the ICs (the periodic wiggles indicated by arrows in Fig. 3d are presumably Fourier transformation artifacts due to limited diffraction angle). The 1st peak of IC1 appears at a distance of Cu–Cu bonds. It is the main constituent of the shear band (Fig. 3e), suggesting a significantly higher Cu concentration in the shear band in line with previous APT results. Moreover, IC1 exhibits very weak features at interatomic distances larger than the nearest neighbors, indicating a reduced medium-range order in the shear band. This observation qualitatively agrees with MD simulations, in which the geometrically favored motifs in the shear band fragment to enable plastic shearing [51]. This is difficult to probe directly by conventional experiments. IC3 reflects a packing of atoms much larger than the other two ICs. Its 1st pronounced peak locates at the same distance as Zr–Zr bonds. The overall features are nearly identical to the Zr–Zr partial PDF obtained in MD simulations (Fig. 3d). Therefore, IC3 is attributed to the Zr–Zr correlation. Its distribution map (Fig. 3g) indicates significantly less Zr–Zr atomic pairs in the shear band, consistent with the large amount of Cu in the shear band. The 1st peak of IC2 is in line with the bond length of Cu–Zr. The envelope of the positive peak between 4.0 and 5.6 Å in IC2 is at the same location as the 2nd peak of Cu–Cu and Cu–Zr MD based partial PDFs and therefore could potentially be attributed to the 2nd-order Cu–Cu and Cu–Zr distances.

PCA picks up the chemical/structural variations in and across the shear band (as shown in the first three PC maps in Figure S8, where the shear band feature can be seen). Following PCA, ICA disentangles the information into elemental specific bond lengths. The Cu/Zr gradient from the shear band to the matrix is presumably the main reason for separating IC1 and IC3 in the PDF dataset and pushing the rest of the atomic correlation information to IC2, which is distributed quite homogeneously, just slightly reduced in the shear band.

The IC maps show a non-uniform distribution in the amorphous matrix, where clusters with a size of a couple nanometers are noticeable, potentially suggesting nanoscale inhomogeneities in the MG. The dimension of the observed structural variations is in good agreement with simulated polyhedral networks [52,53], surface mechanical response mapping [54] and local symmetry mapping [18,19]. APT analysis of this sample [25] also showed the Cu and Zr composition in the glass layer to fluctuate by ~5 at.% with 1 to 2 nm spatial frequency. Of course, a contribution from local preferential orientation of clusters and noise cannot be excluded, considering that the variations are averaged over the 50 nm thick specimen.

### 3.4. Determining number of components

Conventionally, the eigenvalues of the covariance matrix are plotted as a function of component number in a scree plot and

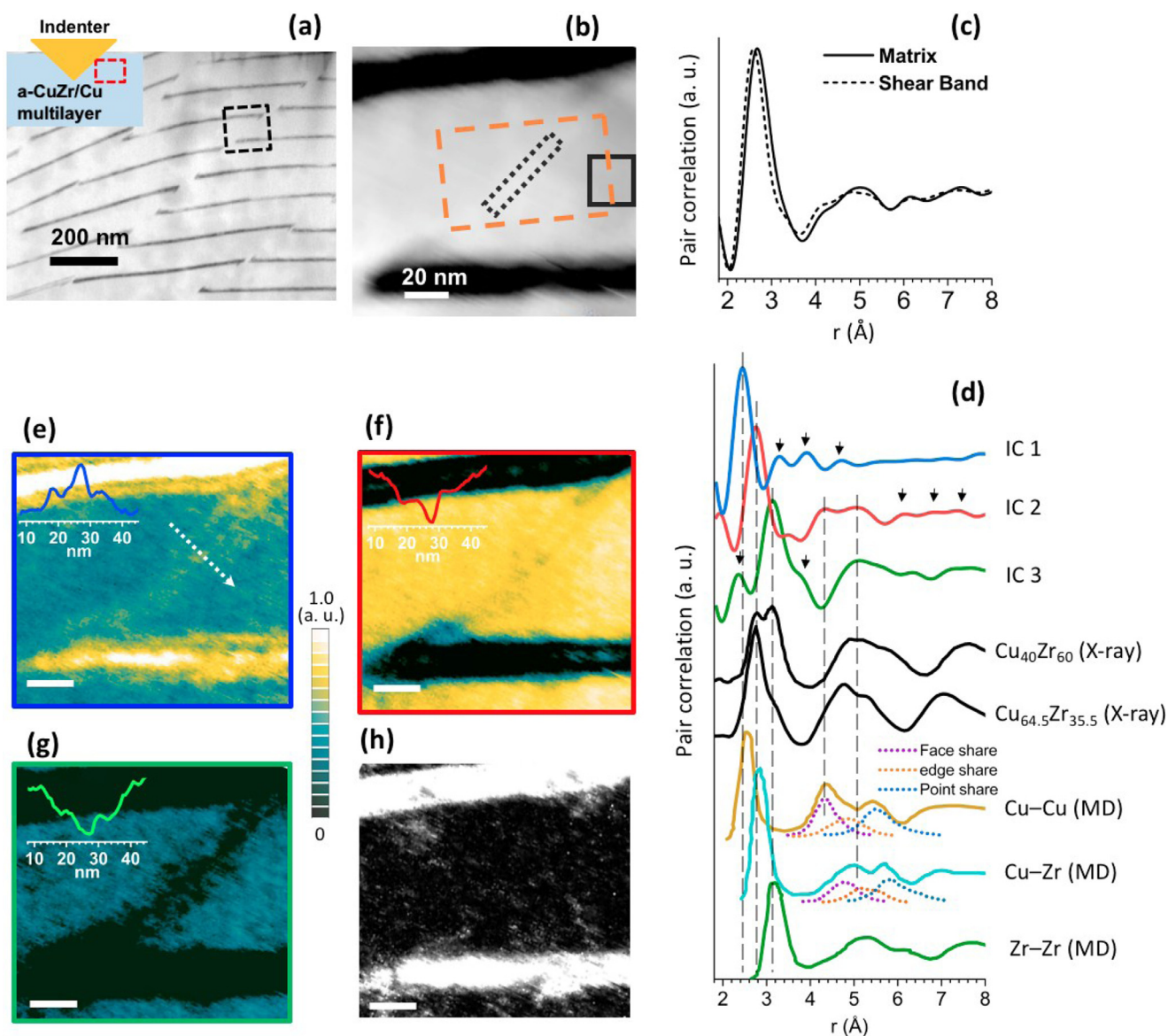


**Fig. 3.** ICA facilitated STEM-PDF characterizing shear band. (a) Sketch of the deformation process of the a-CuZr/c-Cu multilayer by Vickers indentation and STEM-HAADF image of the cross-section of the deformed region corresponding the red dashed box in the sketch. (b) Enlarged view from the area highlighted by the black dashed box in (a). (c) Representative raw PDFs of the amorphous matrix (solid) taken from the glass matrix region of the a-CuZr layer indicated by the black solid box in (b) and representative raw PDF of the shear band (dotted) taken from the black dotted box in (b). (d) ICA results obtained using the PDF data taken from the orange dotted box in (b), and comparison of ICs to experimental X-ray PDFs reproduced from [48] and partial PDFs from MD simulation of  $\text{Cu}_{50}\text{Zr}_{50}$  BMG reproduced from [50]. The black arrows pointing at wiggles are presumably Fourier transformation (TF) artifacts due to the limited recorded diffraction angle. Spatial distribution (IC coefficients) of (e) IC1, (f) IC2 and (g) IC3 in the same contrast level and the intensity is in arbitrary unit. The insets are line profiles along the dashed white arrow in (e). (h) Residual error of the ICA (gray scale), which is mainly concentrated on the c-Cu layer. The length of the white scale bars in (e)–(h) are 20 nm.

the number of significant components in the multi-dimensional hyperspectral data is determined from the ‘elbow’ in the scree plot. The noise exponentially decrease with increasing component order [32], so that the components related to noise will show a linear behavior in the scree plot when plotted on a logarithmic scale. The low-order components above the line therefore are considered as principal components significant compared to the noise. This criterion has been widely used for MSA processing of EELS and EDX spectrum images [33,36,37], and also works well when used for the STEM-PDF data of the  $\text{ZrO}_2/\text{FeZr}$  multilayer (Fig. 1d and Figure S4) because of its simple geometry and limited phase overlap. However, as shown in the scree test of the nanoglass and shear band data in Fig. 4 (linear plot in Figure S9), determining the number of components in case of the nanoglass and the shear band, where complex and strong phase overlap appears, only based on

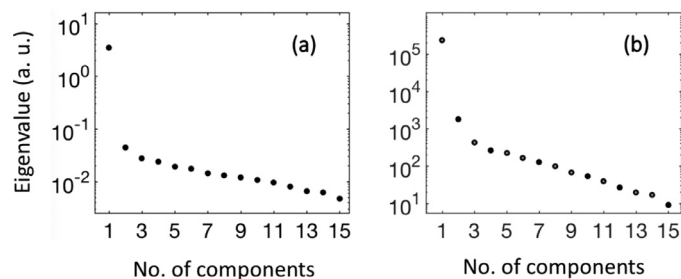


**Fig. 4.** Scree test for (a) the nanoglass dataset (b) the shear band dataset.

the scree plot of eigenvalues is not straightforward. Therefore, we improved the scree test by considering the information in the de-

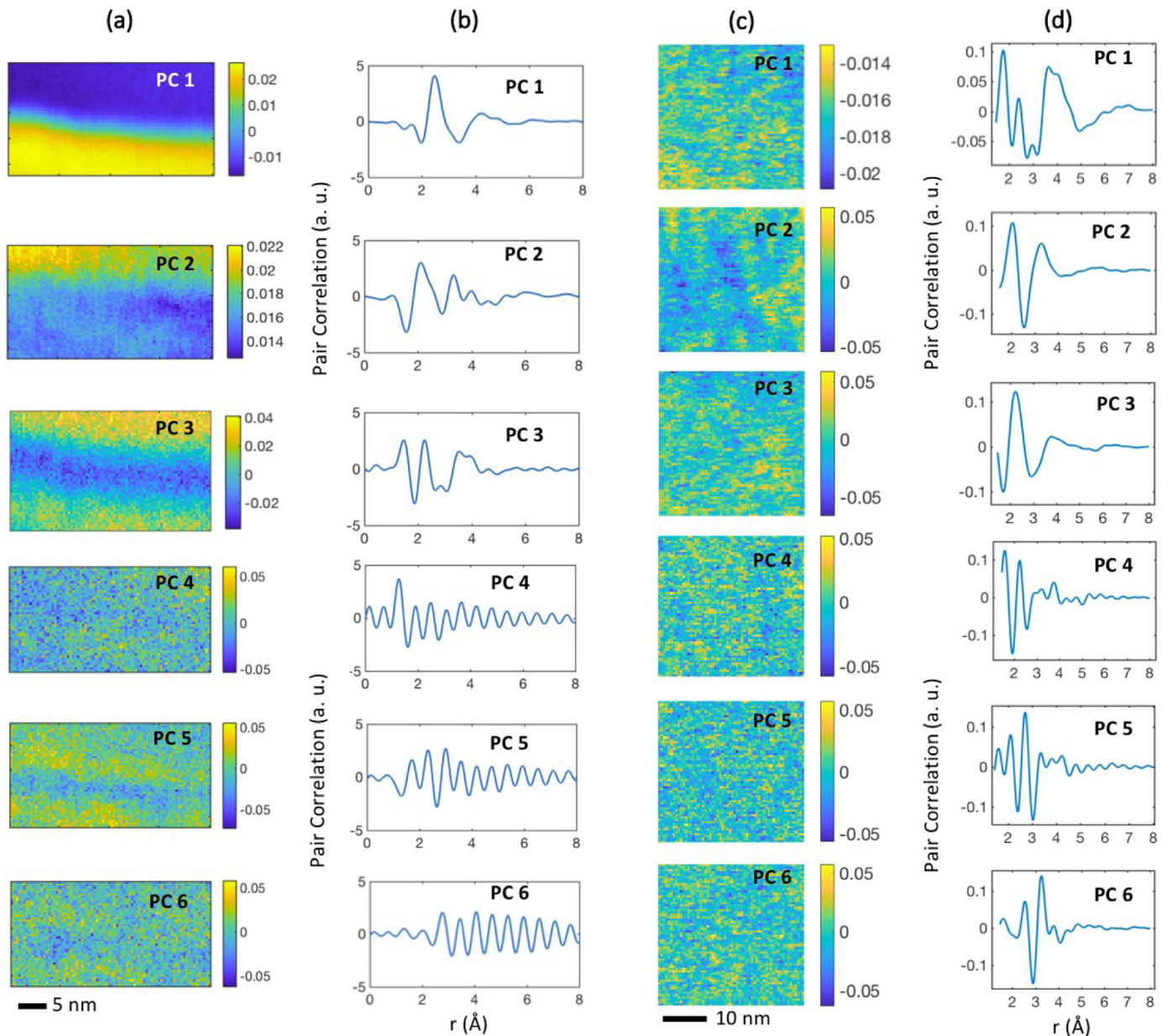


**Fig. 5.** The first 6 components of the PCA results of the ZrO<sub>2</sub>/FeZr multilayer and nanoglass data. (a) Distribution maps (intensities are in arbitrary unit) and (b) corresponding PCs of the ZrO<sub>2</sub>/FeZr multilayer data. (c) Distribution maps and (d) corresponding PCs of the nanoglass data.

whitening matrix and PCs of high-order components. We are going to show in the following that a deeper analysis of these information can confidently determine the number of components.

As an example, the distribution maps (i.e. the columns of the dewhitening matrix) and PC curves of the first 6 PCs of the ZrO<sub>2</sub>/FeZr multilayer data are shown in Fig. 5a and b. The maps of the high-order PCs ( $\geq 4$ ) are dominated by noise-like random fluctuation compared to the maps of the first 3 PCs (though weak features can be seen in the map of PC5 and PC6). The true atomic structure information in the 4D-STEM data should be consistent with the spatial distribution of the phases (i.e. the multilayer-interfacial geometry in this sample). The random-fluctuations in the maps of the higher-order PCs indicate that they do not correspond to meaningful signals, but are due to noise, which is random without correlation to the sample geometry. Furthermore, the PC curves with higher order than three are dominated by high frequency sinusoidal oscillation, which presumably comes from

Fourier transformation of noise at high angles of the structure factor, without any relation to atomic pair distances.

The PCA results of the nanoglass data (Fig. 5c and d) and the shear band data (Figure S8) show the same behavior as the ZrO<sub>2</sub>/FeZr multilayer data. The PC maps are dominated by random noise and the PC curves are dominated by high frequency oscillations starting from the 4th-order PC. Different from the ZrO<sub>2</sub>/FeZr multilayer, the nanoglass does not exhibit a regular morphology of the phase distribution, making an estimation of the randomness of the maps by eye difficult. Therefore, we adopt the concept of information entropy of an image to quantify the randomness of the PC maps following the information theory in image processing [55,56]. For an image, its information entropy is defined as  $H = -\sum_j P_j \ln(P_j)$ , where  $P_j$  is the histogram value of the intensity  $j$  in the image. To eliminate the limitation of this histogram-based quantity for distinguishing global noise from the true information with similar variance, local entropy is used instead of

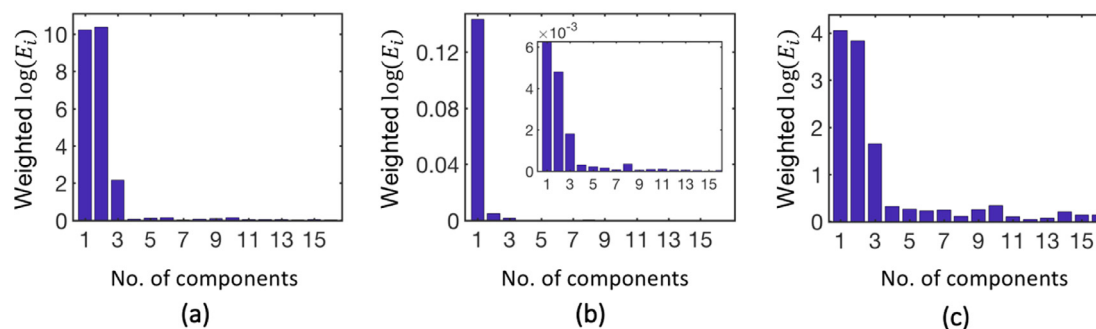


**Fig. 6.** Modified scree test combining eigenvalues (of the covariance matrices) and local entropies (of the dewhitening matrices) for (a) ZrO<sub>2</sub>/FeZr multilayer data, (b) nanoglass data, the inset is vertically enlarged plot, (c) shear band data.

the global entropy. The image is divided into sub-patches and the size of the patches ( $a$ ) is optimized to balance the number of patches and sufficient sampling of pixels in the each patch ( $a = \arg \max_{a^2} \frac{A}{a^2} \ln(a^2 - 2^n)$ ,  $A$  is the size (number of total pixels) of the image,  $n$  is the bit depth of pixel in the image. In the optimization,  $\frac{A}{a^2}$  expects that the number of the patches shall be big enough, and  $(a^2 - 2^n)$  guarantees the sufficient sampling of the histogram comparable to the bit-depth of the image). For the examples in this work (with the same magnitude of total pixel numbers), the PC maps are scaled to 8-bit grayscale corresponding to patch size of 19 pixels. The local entropy  $\bar{H}_i$  of the  $i$ th PC map (i.e. the  $i$ th row of the dewhitening matrix) is then calculated by averaging the entropy of all sub-patches in the map. Smaller  $\bar{H}_i$  means less randomness and therefore more information. The eigenvalue of the  $i$ th PC ( $E_i$ ) are then weighted by  $\bar{H}_i$  for the scree test, through  $E_{i, \text{weighted}} = -\log(\bar{H}_i) \log(E_i/E_{\min})$ , where  $E_{\min}$  as a normalize factor is the smallest eigenvalue among the components used for the scree plot. Fig. 6a shows the modified scree test for the ZrO<sub>2</sub>/FeZr multilayer data. It clearly shows that the first 3 components should be selected as principal components. We then performed the information entropy weighted scree test to the nanoglass (Fig. 6b) and the shear band data (Fig. 6c). The results clearly indicate that the first 3 PCs should be considered to be principal for the following ICA process.

#### 4. Summary and conclusion

We applied PCA/ICA to enhance the capability of STEM-PDF for analyzing amorphous hetero-structures and nanocomposite materials, where the small size and phase overlap impedes conventional characterization methods. As a proof of principle, we analyzed a ZrO<sub>2</sub>/FeZr multilayer and discovered Fe–O bonding and Fe–Fe correlations indicating an iron oxide (Marokite), which is enriched at the interface and also somewhat distributed in the ZrO<sub>2</sub> layer. To illustrate the capabilities to analyze more complex and scientifically more interesting samples, we investigated the structure of a nanoglass and a shear band. The analysis of a Fe<sub>25</sub>Sc<sub>75</sub> nanoglass resulted in three independent phases that are present. Fe partially segregated from the Sc-rich matrix forming a “Fe<sub>10</sub>Sc<sub>90</sub>” phase with Fe–Fe bonding and medium-range order. The analysis of a shear band in a deformed nanolaminate disentangled the Cu–Cu, Cu–Zr and Zr–Zr bonding and their distribution in the shear band and matrix. The analysis does not only confirm the enrichment of Cu in the shear band, but also proved the reduced structural ordering in the shear band. Furthermore, it revealed a nanoscale structural/chemical inhomogeneity of the CuZr metallic glass.

Our work opens the door to characterize heterogeneous amorphous materials using the multi-dimensional local diffraction data. The combination of STEM-PDF and MSA techniques is a key to unlock vast additional information. ICA was used in this work, other

type MSA methods e.g. Bayesian demixing [57] and cluster analysis [58,59] could be alternative MSA approaches. As demonstrated by the three representative examples that are often encountered in material science research, this approach can disentangle the mixed information among nanophases and discover minor phases hidden in overlapping data, giving material scientists significantly improved capacity for understanding amorphous materials. Moreover, the atomic structure may be anisotropic in some cases (e.g. in the deformed regions or at special boundaries), where PDF analysis considering high-order spherical harmonic components of the diffraction rings [60] could potentially be integrated for providing information on the local structural anisotropy. It is worth to note that using ICA to analyze STEM-PDF data minimizes the demand for preexisting knowledge about the material. In particular, it does not require any reference data for the individual phases in the composite, which is difficult to obtain in many cases. It also suppresses biased judgment, which commonly happens by manual analysis of the data. Moreover, the concrete information of local bonding and atomic coordination can be readily interpreted compared to the fairly vague “short- or medium-range order” which have to rely on simulation-based structure modeling for interpretation. It is expected that this method can be directly applied to investigate a wide range of material questions involving amorphous structures, such as organic composites, chemical or physical induced amorphization processes in addition to the nanoglasses and shear bands investigated here.

#### Content of supporting information

STEM-PDF data processing procedure with real data of the measured samples; Scree plot in linear scale of y-axis; conventional STEM-HAADF, EELS analysis of the FeSc nanoglass sample; Detailed PCA results of the shear band data.

#### Declaration of Competing Interest

The authors declare that they have no known competing financial interests or personal relationships that could have appeared to influence the work reported in this paper.

#### Acknowledgments

Authors thank Prof. T. Feng (Nanjing University of Science and Technology) for providing the TEM lamella of the ZrO<sub>2</sub>/FeZr multilayer and the FeSc melt spun ribbons, and Dr. W. Guo (Headway Technologies, Inc.) for providing the indented a-CuZr/c-Cu nanolaminate. Authors acknowledge Dr. M. Hammad (INT, KIT) and Dr. S. Schlöblich (INT, KIT) for FIB preparation of the TEM lamellae. XM thanks the Deutsche Forschungsgemeinschaft’s for funding of grant MU 4276/1-1 for the financial support.

## References

- [1] C. Schuh, T. Hufnagel, U. Ramamurty, Mechanical behavior of amorphous alloys, *Acta Mater* 55 (2007) 4067–4109, doi:[10.1016/j.actamat.2007.01.052](https://doi.org/10.1016/j.actamat.2007.01.052).
- [2] A.L. Greer, Y.Q. Cheng, E. Ma, Shear bands in metallic glasses, *Mater. Sci. Eng. R Rep.* 74 (2013) 71–132, doi:[10.1016/j.mser.2013.04.001](https://doi.org/10.1016/j.mser.2013.04.001).
- [3] Y.M. Chen, T. Ohkubo, T. Mukai, K. Hono, Structure of shear bands in Pd 40 Ni 40 P 20 bulk metallic glass, *J. Mater. Res.* 24 (2009) 1–9, doi:[10.1557/JMR.2009.0001](https://doi.org/10.1557/JMR.2009.0001).
- [4] H. Rösner, M. Peterlechner, C. Kübel, V. Schmidt, G. Wilde, Density changes in shear bands of a metallic glass determined by correlative analytical transmission electron microscopy, *Ultramicroscopy* 142 (2014) 1–9, doi:[10.1016/j.ultramic.2014.03.006](https://doi.org/10.1016/j.ultramic.2014.03.006).
- [5] H. Gleiter, Nanoglasses: a new kind of noncrystalline materials, *Beilstein J. Nanotechnol.* 4 (2013) 517–533, doi:[10.3762/bjnano.4.61](https://doi.org/10.3762/bjnano.4.61).
- [6] Y. Ivanisenko, C. Kübel, S.H. Nandam, C. Wang, X. Mu, O. Adjaoud, K. Albe, H. Hahn, Structure and properties of nanoglasses, *Adv. Eng. Mater.* 1800404 (2018) 1–16, doi:[10.1002/adem.201800404](https://doi.org/10.1002/adem.201800404).
- [7] R. Witte, T. Feng, J.X. Fang, A. Fischer, M. Ghafari, R. Kruk, R. A. Brand, D. Wang, H. Hahn, H. Gleiter, Evidence for enhanced ferromagnetism in an iron-based nanoglass, *Appl. Phys. Lett.* 103 (2013) 73106, doi:[10.1063/1.4818493](https://doi.org/10.1063/1.4818493).
- [8] C. Wang, M. Palit, N. Yin, Q. Shi, Y. Ivanisenko, H. Gleiter, H. Hahn, Magnetic contributions to the low-temperature specific heat of Sc79Fe21 nanoglass, *J. Appl. Phys.* 125 (2019) 45111, doi:[10.1063/1.5082579](https://doi.org/10.1063/1.5082579).
- [9] D. Şopu, Y. Ritter, H. Gleiter, K. Albe, Deformation behavior of bulk and nanostructured metallic glasses studied via molecular dynamics simulations, *Phys. Rev. B* 83 (2011) 100202, doi:[10.1103/PhysRevB.83.100202](https://doi.org/10.1103/PhysRevB.83.100202).
- [10] O. Adjaoud, K. Albe, Interfaces and interphases in nanoglasses: surface segregation effects and their implications on structural properties, *Acta Mater* 113 (2016) 284–292, doi:[10.1016/j.actamat.2016.05.002](https://doi.org/10.1016/j.actamat.2016.05.002).
- [11] T. Egami, S.J. Billinge, *Underneath the Bragg Peaks Structural Analysis of Complex Materials*, second ed., Elsevier Ltd, Kidlington, Oxford OX5 1GB, UK, 2003.
- [12] D.J.H. Cockayne, D.R. McKenzie, Electron diffraction analysis of polycrystalline and amorphous thin films, *Acta Crystallogr. A* 44 (1988) 870–878, doi:[10.1107/S0108767388004957](https://doi.org/10.1107/S0108767388004957).
- [13] T.E. Gorelik, R. Neder, M.W. Terban, Z. Lee, X. Mu, C. Jung, T. Jacob, U. Kaiser, Towards quantitative treatment of electron pair distribution function, *Acta Crystallogr. Sect. B* 75 (2019) 532–549, doi:[10.1107/S205252061900670X](https://doi.org/10.1107/S205252061900670X).
- [14] M.M.J. Treacy, J.M. Gibson, L. Fan, D.J. Paterson, I. McNulty, Fluctuation microscopy: a probe of medium range order, *Rep. Prog. Phys.* 68 (2005) 2899–2944, doi:[10.1088/0034-4885/68/12/R06](https://doi.org/10.1088/0034-4885/68/12/R06).
- [15] V. Schmidt, H. Rösner, M. Peterlechner, G. Wilde, P.M. Voyles, Quantitative measurement of density in a shear band of metallic glass monitored along its propagation direction, *Phys. Rev. Lett.* 115 (2015) 35501, doi:[10.1103/PhysRevLett.115.035501](https://doi.org/10.1103/PhysRevLett.115.035501).
- [16] J. Hwang, Z.H. Melgarejo, Y.E. Kalay, I. Kalay, M.J. Kramer, D.S. Stone, P.M. Voyles, Nanoscale structure and structural relaxation in Zr50Cu45Al5 bulk metallic glass, *Phys. Rev. Lett.* 108 (2012) 195505, doi:[10.1103/PhysRevLett.108.195505](https://doi.org/10.1103/PhysRevLett.108.195505).
- [17] M.M.J. Treacy, K.B. Borisenko, The local structure of amorphous silicon, *Science* 335 (2012) 950–953, doi:[10.1126/science.1214780](https://doi.org/10.1126/science.1214780).
- [18] S. Im, Z. Chen, J.M. Johnson, P. Zhao, G.H. Yoo, E.S. Park, Y. Wang, D.A. Muller, J. Hwang, Direct determination of structural heterogeneity in metallic glasses using four-dimensional scanning transmission electron microscopy, *Ultramicroscopy* 195 (2018) 189–193, doi:[10.1016/j.ultramic.2018.09.005](https://doi.org/10.1016/j.ultramic.2018.09.005).
- [19] A.C.Y. Liu, M.J. Neish, G. Stokol, G.A. Buckley, L.A. Smillie, M.D. de Jonge, R.T. Ott, M.J. Kramer, L. Bourgeois, Systematic mapping of icosahedral short-range order in a melt-spun Zr36Cu64 metallic glass, *Phys. Rev. Lett.* 110 (2013) 205505, doi:[10.1103/PhysRevLett.110.205505](https://doi.org/10.1103/PhysRevLett.110.205505).
- [20] X. Mu, D. Wang, T. Feng, C. Kübel, Radial distribution function imaging by STEM diffraction: phase mapping and analysis of heterogeneous nanostructured glasses, *Ultramicroscopy* 168 (2016) 1–6, doi:[10.1016/j.ultramic.2016.05.009](https://doi.org/10.1016/j.ultramic.2016.05.009).
- [21] X. Mu, A. Mazilkin, C. Sprau, A. Colsmann, C. Kübel, Mapping structure and morphology of amorphous organic thin films by 4D-STEM pair distribution function analysis, *Microscopy* 68 (2019) 301–309, doi:[10.1093/jmicro/dfz015](https://doi.org/10.1093/jmicro/dfz015).
- [22] X. Mu, S. Neelamraju, W. Sigle, C.T. Koch, N. Totò, J.C. Schön, A. Bach, D. Fischer, M. Jansen, P.A. van Aken, Evolution of order in amorphous-to-crystalline phase transformation of MgF<sub>2</sub>, *J. Appl. Crystallogr.* 46 (2013) 1105–1116, doi:[10.1107/S0021889813011345](https://doi.org/10.1107/S0021889813011345).
- [23] G. Anstis, Z. Liu, M. Lake, Investigation of amorphous materials by electron diffraction—The effects of multiple scattering, *Ultramicroscopy* 26 (1988) 65–70, doi:[10.1016/0304-3991\(88\)90378-6](https://doi.org/10.1016/0304-3991(88)90378-6).
- [24] D.R.G. Mitchell, Determination of mean free path for energy loss and surface oxide film thickness using convergent beam electron diffraction and thickness mapping: a case study using Si and P91 steel, *J. Microsc.* 224 (2006) 187–196, doi:[10.1111/j.1365-2818.2006.01690.x](https://doi.org/10.1111/j.1365-2818.2006.01690.x).
- [25] W. Guo, E.A. Jägle, P.-P. Choi, J. Yao, A. Kostka, J.M. Schneider, D. Raabe, Shear-induced mixing governs co deformation of crystalline-amorphous nanolaminates, *Phys. Rev. Lett.* 113 (2014) 35501, doi:[10.1103/PhysRevLett.113.035501](https://doi.org/10.1103/PhysRevLett.113.035501).
- [26] E.F. Rauch, J. Portillo, S. Nicolopoulos, D. Bultreys, S. Rouvimov, P. Moeck, Automated nanocrystal orientation and phase mapping in the transmission electron microscope on the basis of precession electron diffraction, *Z. Krist.* 225 (2010) 103–109, doi:[10.1524/zkri.2010.1205](https://doi.org/10.1524/zkri.2010.1205).
- [27] J. Ankele, J. Mayer, P. Lamparter, S. Steeb, Quantitative electron diffraction data of amorphous materials, *Z. Naturforsch* 60a (2005) 459–468, doi:[10.1515/zna-2005-0612](https://doi.org/10.1515/zna-2005-0612).
- [28] W. McBride, D.J.H. Cockayne, C. Goringe, Reduced density function analysis using convergent electron illumination and iterative blind deconvolution, *Ultramicroscopy* 76 (1999) 115–123, doi:[10.1016/S0304-3991\(98\)00082-5](https://doi.org/10.1016/S0304-3991(98)00082-5).
- [29] W. McBride, D.J.H. Cockayne, K. Tsuda, Deconvolution of electron diffraction patterns of amorphous materials formed with convergent beam, *Ultramicroscopy* 94 (2003) 305–308, doi:[10.1016/S0304-3991\(02\)00340-6](https://doi.org/10.1016/S0304-3991(02)00340-6).
- [30] W. McBride, D.J.H. Cockayne, The structure of nanovolumes of amorphous materials, *J. Non-Crystalline Solids* 318 (2003) 233–238, doi:[10.1016/S0022-3093\(02\)01908-7](https://doi.org/10.1016/S0022-3093(02)01908-7).
- [31] A. Hyvärinen, E. Oja, Independent component analysis: algorithms and applications, *Neural Netw.* 13 (2000) 411–430, doi:[10.1016/S0893-6080\(00\)00026-5](https://doi.org/10.1016/S0893-6080(00)00026-5).
- [32] N. Bonnet, N. Brun, C. Colliex, Extracting information from sequences of spatially resolved EELS spectra using multivariate statistical analysis, *Ultramicroscopy* 77 (1999) 97–112, doi:[10.1016/S0304-3991\(99\)00042-X](https://doi.org/10.1016/S0304-3991(99)00042-X).
- [33] M. Bosman, M. Watanabe, D.T.L. Alexander, V.J. Keast, Mapping chemical and bonding information using multivariate analysis of electron energy-loss spectrum images, *Ultramicroscopy* 106 (2006) 1024–1032, doi:[10.1016/j.ultramic.2006.04.016](https://doi.org/10.1016/j.ultramic.2006.04.016).
- [34] P.G. Kotula, M.R. Keenan, Application of multivariate statistical analysis to STEM X-ray spectral images: interfacial analysis in microelectronics, *Microsc. Microanal.* 12 (2006) 538–544, doi:[10.1017/S1431927606006036](https://doi.org/10.1017/S1431927606006036).
- [35] P. Lu, B.D. Gauntt, Structural mapping of disordered materials by nanobeam diffraction imaging and multivariate statistical analysis, *Microsc. Microanal.* 19 (2013) 300–309, doi:[10.1017/S1431927613000135](https://doi.org/10.1017/S1431927613000135).
- [36] F. de la Peña, M.H. Berger, J.F. Hochepeid, F. Dynys, O. Stephan, M. Walls, Mapping titanium and tin oxide phases using EELS: an application of independent component analysis, *Ultramicroscopy* 111 (2011) 169–176, doi:[10.1016/j.ultramic.2010.10.001](https://doi.org/10.1016/j.ultramic.2010.10.001).
- [37] F. de la Peña, E. Prestat, V.T. Fauske, P. Burdet, P. Jokubauskas, M. Nord, T. Ostasevicius, K.E. MacArthur, M. Sarahan, D.N. Johnstone, J. Taillon, J. Lähnemann, V. Migunov, A. Eljarrat, J. Caron, T. Aarholt, S. Mazzucco, M. Walls, T. Slater, F. Winkler, Pquinn-Dls, B. Martineau, G. Donval, R. McLeod, E.R. Hoglund, I. Alxneit, D. Lundebj, T. Henninen, L.F. Zagonel, A. Garmannslund, Hyperspy v1.5.2, Zenodo, <https://hyperspy.org>. (n.d.). doi: 10.5281/ZENODO.592838.
- [38] D.D. Lee, H.S. Seung, Learning the parts of objects by non-negative matrix factorization, *Nature* 401 (1999) 788–791, doi:[10.1038/44565](https://doi.org/10.1038/44565).
- [39] A.S. Eggeman, R. Krakow, P.A. Midgley, Scanning precession electron tomography for three-dimensional nanoscale orientation imaging and crystallographic analysis, *Nat. Commun.* 6 (2015) 7267, doi:[10.1038/ncomms52267](https://doi.org/10.1038/ncomms52267).
- [40] Y. Fei, D.J. Frost, H.-K. Mao, C.T. Prewitt, D. Haeusermann, In situ structure determination of the high-pressure phase of Fe<sub>3</sub>O<sub>4</sub>, *Am. Mineral.* 84 (1999) 203–206, doi:[10.2138/am-1999-1-222](https://doi.org/10.2138/am-1999-1-222).
- [41] X.L. Wang, F. Jiang, H. Hahn, J. Li, H. Gleiter, J. Sun, J.X. Fang, Plasticity of a scandium-based nanoglass, *Scr. Mater.* 98 (2015) 40–43, doi:[10.1016/j.scriptamat.2014.11.010](https://doi.org/10.1016/j.scriptamat.2014.11.010).
- [42] X.J. Liu, P. Yu, C.P. Wang, K. Ishida, Thermodynamic evaluation of the Co–Sc and Fe–Sc systems, *J. Alloys Compd.* 466 (2008) 169–175, doi:[10.1016/j.jallcom.2007.11.069](https://doi.org/10.1016/j.jallcom.2007.11.069).
- [43] J.Y. Kim, D. Jang, J.R. Greer, Nanolaminates utilizing size-dependent homogeneous plasticity of metallic glasses, *Adv. Funct. Mater.* 21 (2011) 4550–4554, doi:[10.1002/adfm.201101164](https://doi.org/10.1002/adfm.201101164).
- [44] Y. Wang, J. Li, A.V. Hamza, T.W. Barbee, Ductile crystalline-amorphous nanolaminates, *Proc. Natl. Acad. Sci.* 104 (2007) 11155–11160, doi:[10.1073/pnas.0702344104](https://doi.org/10.1073/pnas.0702344104).
- [45] D. Şopu, A. Stukowski, M. Stoica, S. Scudino, Atomic-level processes of shear band nucleation in metallic glasses, *Phys. Rev. Lett.* 119 (2017) 195503, doi:[10.1103/PhysRevLett.119.195503](https://doi.org/10.1103/PhysRevLett.119.195503).
- [46] V. Hieronymus-Schmidt, H. Rösner, G. Wilde, A. Zaccane, Shear banding in metallic glasses described by alignments of Eshelby quadrupoles, *Phys. Rev. B* 95 (2017) 134111, doi:[10.1103/PhysRevB.95.134111](https://doi.org/10.1103/PhysRevB.95.134111).
- [47] N. Mattern, A. Schöps, U. Kühn, J. Acker, O. Khvostikova, J. Eckert, Structural behavior of CuxZr100-x metallic glass (x = 35–70), *J. Non-Crystalline Solids* 354 (2008) 1054–1060, doi:[10.1016/j.jnoncrysol.2007.08.035](https://doi.org/10.1016/j.jnoncrysol.2007.08.035).
- [48] D. Ma, A.D. Stoica, X.-L. Wang, Z.P. Lu, M. Xu, M. Kramer, Efficient local atomic packing in metallic glasses and its correlation with glass-forming ability, *Phys. Rev. B* 80 (2009) 14202, doi:[10.1103/PhysRevB.80.014202](https://doi.org/10.1103/PhysRevB.80.014202).
- [49] S. Marinier, L.J. Lewis, Femtosecond laser ablation of CuxZr1-x bulk metallic glasses: a molecular dynamics study, *Phys. Rev. B* 92 (2015) 184108, doi:[10.1103/PhysRevB.92.184108](https://doi.org/10.1103/PhysRevB.92.184108).
- [50] S.P. Pan, J.Y. Qin, W.M. Wang, T.K. Gu, Origin of splitting of the second peak in the pair-distribution function for metallic glasses, *Phys. Rev. B* 84 (2011) 92201, doi:[10.1103/PhysRevB.84.092201](https://doi.org/10.1103/PhysRevB.84.092201).
- [51] A.J. Cao, Y.Q. Cheng, E. Ma, Structural processes that initiate shear localization in metallic glass, *Acta Mater.* 57 (2009) 5146–5155, doi:[10.1016/j.actamat.2009.07.016](https://doi.org/10.1016/j.actamat.2009.07.016).
- [52] J. Ding, Y.Q. Cheng, E. Ma, Full icosahedra dominate local order in Cu64Zr34 metallic glass and supercooled liquid, *Acta Mater.* 69 (2014) 343–354, doi:[10.1016/j.actamat.2014.02.005](https://doi.org/10.1016/j.actamat.2014.02.005).
- [53] J. Ding, S. Patinet, M.L. Falk, Y. Cheng, E. Ma, Soft spots and their structural signature in a metallic glass, *Proc. Natl. Acad. Sci.* 111 (2014) 14052–14056, doi:[10.1073/pnas.1412095111](https://doi.org/10.1073/pnas.1412095111).
- [54] Y.H. Liu, D. Wang, K. Nakajima, W. Zhang, A. Hirata, T. Nishi, A. Inoue, M.W. Chen, Characterization of nanoscale mechanical heterogeneity in a

- metallic glass by dynamic force microscopy, *Phys. Rev. Lett.* 106 (2011) 125504, doi:[10.1103/PhysRevLett.106.125504](https://doi.org/10.1103/PhysRevLett.106.125504).
- [55] G. Rafael, C.W. Richard, E.E.L. Steven, *Digital Image Processing Using MATLAB, third ed.*, Gatesmark Publishing, 2020.
- [56] C. Yan, N. Sang, T. Zhang, Local entropy-based transition region extraction and thresholding, *Pattern Recognit. Lett.* 24 (2003) 2935–2941, doi:[10.1016/S0167-8655\(03\)00154-5](https://doi.org/10.1016/S0167-8655(03)00154-5).
- [57] E. Strelcov, A. Belianinov, Y.H. Hsieh, S. Jesse, A.P. Baddorf, Y.H. Chu, S.V. Kalinin, Deep data analysis of conductive phenomena on complex oxide interfaces: Physics from data mining, *ACS Nano* 8 (2014) 6449–6457, doi:[10.1021/nn502029b](https://doi.org/10.1021/nn502029b).
- [58] D.S.B. Everitt, S. Landau, M. Leese, *Cluster Analysis, fifth ed.*, John Wiley & Sons Ltd, Chichester, West Sussex, UK, 2011.
- [59] J.C. Bezdek, R. Ehrlich, W. Full, FCM: the fuzzy c-means clustering algorithm, *Comput. Geosci.* 10 (1984) 191–203, doi:[10.1016/0098-3004\(84\)90020-7](https://doi.org/10.1016/0098-3004(84)90020-7).
- [60] W. Dmowski, T. Iwashita, C.-P. Chuang, J. Almer, T. Egami, Elastic heterogeneity in metallic glasses, *Phys. Rev. Lett.* 105 (2010) 205502, doi:[10.1103/PhysRevLett.105.205502](https://doi.org/10.1103/PhysRevLett.105.205502).